IEEE Access
Multidisciplinary | Rapid Review | Open Access Journal

Received June 6, 2021, accepted August 2, 2021, date of publication August 5, 2021, date of current version August 17, 2021.

Digital Object Identifier 10.1109/ACCESS.2021.3102631

Power-Synchronized Grid-Following Inverter Without a Phase-Locked Loop

BEHROOZ BAHRANI, (Senior Member, IEEE)
Department of Electrical and Computer Systems Engineering, Monash University, Clayton, VIC 3800, Australia
e-mail: behrooz.bahrani@monash.edu

This work was supported by Australian Renewable Energy Agency (ARENA) through the Advancing Renewable Program under Grant 2020/ARP007.

ABSTRACT This paper proposes a power-synchronized control strategy for grid-following inverters (GFLIs) to regulate their power exchange with the grid without any need for sensing/regulating the point of connection voltage. Contrary to conventional GFLIs, which rely on phase-locked loops for grid synchronization and have difficulties in weak grid conditions, the proposed strategy is power synchronized and utilizes the inverter terminal voltage for power control leading to its seamless performance in ultra-weak grids. Additionally, since the proposed approach does not require any voltage regulation at the point of connection to the grid, contrary to grid-forming inverters, it can reliably operate in stiff and/or series-compensated grids as well. The proposed approach benefits from a decoupling control structure that is tuned using a loop-shaping method. Compared to conventional GFLIs, this approach does not need any extra hardware; hence, it can easily be retrofitted into the existing large fleet of GFLIs. The performance of the proposed controller is evaluated in Matlab/PLECS for both weak and stiff grids, and the findings are experimentally validated in a scaled-down setup.

INDEX TERMS Grid-following inverters, grid-forming inverters, phase-locked loop, power control, power synchronization, vector current control.

I. INTRODUCTION

Thanks to the increasing climate change concerns and accelerated decline in renewable energy costs, inverter-based resources (IBRs) are rapidly displacing synchronous generators in various power systems around the globe. To export energy, IBRs need to get synchronized with the grid. Their synchronization, however, is primarily based on control algorithms and differs from swing-equation-based synchronization of synchronous generators.

Based on their grid synchronization, two main categories of IBRs exist: 1) grid-following inverters (GFLIs) and 2) grid-forming inverters (GFMIs). GFLIs mainly rely on measuring or estimating the point of connection (PoC) voltage to get synchronized with the grid [1]–[4]. Sensing/estimating the PoC voltage, its phase-angle and frequency are extracted by a phase-locked loop (PLLs), which are then used by a vector current controller [5]–[7]. GFMIs, however, exploit active power-frequency droop control for grid synchronization, [8]–[12]. GFMIs regulate the PoC voltage while the frequency and magnitude of this voltage is provided by active and reactive power control loops, which mainly operate based on droop control. The first category is called grid-following as they follow the PoC voltage by a PLL, while the second one is called grid-forming as they form the voltage of the PoC [13].

GFLIs can seamlessly operate in strong grids and export their maximum power. However, as they rely on PLLs, their performance in weak grids deteriorates, and operation in very weak grids can lead to their instability or side-band oscillations [13]–[16]. These side-band oscillations are mainly due to the asymmetrical control dynamics of synchronous reference frame PLLs. To mitigate the issues PLL face in weak grids, several strategies are proposed. A symmetrical PLL that provides phase-angles in both d- and q-axes is proposed in [17]. Embedding a virtual impedance in the PLL structure, the PLL is synchronized with a remote, strong grid in [1], [18]. Using a band-pass filter, the negative resistance of the PLL is damped by tuning the filter in [19]. In [20], using a feed-forward loop from the PLL to the current control loop,

The associate editor coordinating the review of this manuscript and approving it for publication was Suman Maiti.

symmetrical dynamics in the d- and q-axes are achieved. All of these approaches, however, rely on a PLL and require the PoC voltage measurement.

GFMIs, on the other hand, face stability issues when operating in stiff grids [13]. The main reason is regulating the PoC voltage in stiff grids is challenging as the PoC and the grid are electronically close to each other [21], [22]. Two types of synchronization instability exist for GFMIs: 1) side-band oscillations and 2) synchronous oscillations. To mitigate side-band and synchronous oscillations in GFMIs, several strategies are proposed [23], [24]. Additionally, GFMIs cause side-band oscillations in series-compensated, weak grids [25]. A current feed-forward control added to the modulation voltage is adopted to mitigate these oscillations in series-compensated grids in [25]. In addition to these stability issues, GFMIs performance upon fault recovery poses various challenges as their current needs to be limited to protect their semiconductors switches [26].

In the recent literature, several approaches for PLL-less operation of GFLIs, mainly based on direct power control (DPC), have been proposed. A DPC strategy without any inner current loop has been proposed in [27]. This approach, however, does not provide mechanism to limit the current due to lack of an inner current and also results in a variable switching frequency, causing an unexpected broadband harmonic spectrum range. To ensure a constant switching frequency, other variants of the DPC have been proposed that use space vector modulation [28], or calculate the inverter voltage error in each switching period [29]. Model predictive control-based (MPC)-DPC approaches, which consider system constraints and nonlinearities, are also proposed to achieve constant switching frequency [30], [31]. However, MPC-DPC methods result in an excessive computational burden.

A voltage-modulated DPC (VMDPC) for IBRs is proposed in [32]–[34]. This approach does not require a PLL for its synchronization while it has the same control structure as the conventional vector current control approaches. As its synchronization is not dependent on a PLL, the VMDPC does not suffer from the shortcomings of conventional GFLIs. However, since the VMDPC still requires the PoC voltage to control the power exchange with the grid, its performance in weak grids is deteriorated [34]. The reason is that in weak grids, power injection by the IBR significantly affects the PoC voltage, which in turn can destabilize the system. Although the VMDPC, compared to other DPC-based solutions, provide superior performance, a detailed comparison between the VMDPC and the conventional PLL-based vector current controller reveals that the VMDPC does not provide much of improvement compared to PLL-based methods, in particular, in weak grid conditions [35].

This paper proposes a power-synchronized control strategy for grid-following IBRs that, similar to the VMDPC, does not rely on a PLL to get synchronized with the grid. However, contrary to the VMDPC and many other synchronization techniques, including conventional GFLIs and GFMIs, the proposed method does not require PoC voltage regulation, sensing, or estimation, and it can stably operate in both weak and stiff grids. To avoid complications caused by PoC voltage sensing, the proposed controller utilizes the inverter terminal voltage and controls the power at the terminal of the IBR. To control the real/reactive power exchange, the proposed approach relies on a cascade control architecture whose outer power loop provides the grid frequency and the reference of its inner current control loop. The inner current loop is in place to ensure current limitation if needed. Hence, the main contribution of this paper is proposing a power-synchronized grid-following inverter that

- does not require a PLL,
- does not require PoC voltage sensing (unless used for fault detection) or PoC voltage regulation,
- provides decoupled real/reactive power control,
- can limit its injected current for protection purposes,
- can operate in ultra-weak/stiff grids,
- can replace the existing large fleet of conventional GFLIs.

The rest of this paper is structured as follows. Section II presents an overview of the conventional GFLI and GFMI control strategies. Section III describes the proposed control approach, and its performance is evaluated in Section IV. Finally, the conclusions are provided in Section V.

II. GRID-FOLLOWING VS GRID-FORMING INVERTERS

The block diagram of a conventional GFLI is shown in Fig. 1 in which an IBR is connected to the grid via its filter. The filter is represented by an inductor, $L_{\rm f}$, and its series resistance, $R_{\rm f}$. The grid is represented by an ideal voltage source, and a series inductance and resistance, $L_{\rm g}$ and $R_{\rm g}$, respectively. The main purpose of the GFLI topology is to regulate its power exchange with the grid. This is typically carried out via a vector current controller whose references, i.e., $I_{\rm dq,ref}$, are provided by external power control loops. The vector current controller requires the phase-angle of the grid to which it is interfaced to convert the inverter current to a dq-frame. In GFLIs, a PLL provides the phase-angle of the grid voltage at the PoC. The most common PLL is the synchronous reference frame PLL, which forces the q-component of the PoC voltage to zero leading to decoupled real and reactive power control. That is, the real power depends on the d-component

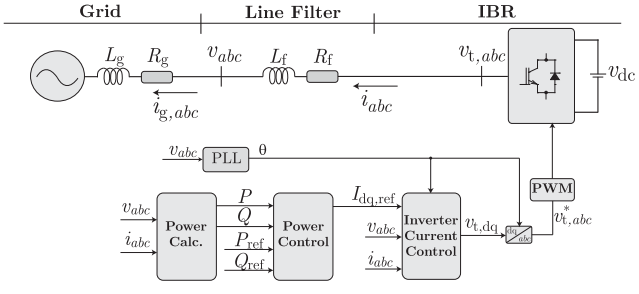

FIGURE 1. A conventional grid-following inverter and its control block diagrams.

of the current, while the reactive power depends on its q-component.

The block diagram of a GFMI is shown in Fig. 2 whose circuitry is similar to the GFLI, while the inverter filter includes an extra capacitor. The GFMI control strategy, however, does not rely on a PLL for grid synchronization. As shown in Fig. 2, a primary control level, mainly based on droop or virtual synchronous generator concepts [8], [36], [37], provides the grid frequency, which is then integrated to calculate the phase-angle required for Park transformation. Additionally, the primary control level provides capacitor voltage references, i.e., $V_{\mathrm{dq,ref}}$, for an internal voltage control loop. The voltage control loop then provides the references for the inverter vector current control loop, which is identical to the vector current control loop of the GFLI. The main differences between the GFLI and GFMI control strategies are their synchronization mechanism and also the existence of a voltage control loop in the GFMI. From the hardware point of view, the GFMI topology typically requires a capacitor connected at the PoC, while this capacitor is not mandatory for the GFLI topology. However, GFLIs often have this capacitor at the PoC, mainly for voltage filtering as they require the PoC voltage for grid synchronization. Note that the current control of the GFMI (and GFLI if equipped with an LCL filter) needs to damp the LC resonance [6].

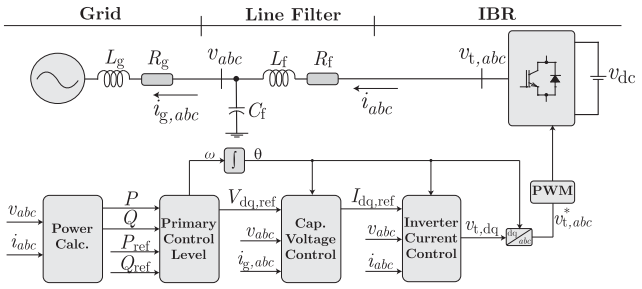

FIGURE 2. A typical grid-forming inverter and its control block diagrams.

The vast majority of currently installed IBRs are GFLIs, which are known for their less-than-stellar performance in weak grids. Although GFMI controllers can seamlessly operate in weak grid conditions, retrofitting the existing large fleet of GFLI IBRs with the GFMI concept is not an easy task as in addition to upgrading the control platform, GFMIs require a capacitor for voltage control, which is not always present in the existing GFLIs. Additionally, GFMIs could exhibit stability issues in stiff and/or series-compensated grids [13]. To address these issues, in the following section, combining certain features of GFLIs and GFMIs, a control strategy for IBRs is proposed that does not require any PoC voltage sensing/regulation for its operation. The proposed controller is power synchronized, and it relies on the inverter terminal voltage and current to regulate power exchange with the grid. Since this approach does not regulate the voltage at the PoC, it is not categorized as a GFMI, although it exploits power synchronization concept similar to conventional GFMIs. However, as the proposed controller requires a grid to follow for its operation, it may be categorized as a grid-following approach.

III. PROPOSED POWER-SYNCHRONIZED INVERTER

The proposed power-synchronized inverter and its control strategy are shown in Fig. 3 in which an IBR is interfaced to the grid via an inductor. As the PoC voltage is not required for this control strategy, either L or LCL filters can be utilized, i.e., a capacitor is not necessarily installed at the PoC. The proposed controller operates in a rotating reference frame aligned with the inverter current, i.e., the q-component of the inverter current is zero. A power calculator block, based on the instantaneous power theory, calculates the power delivered by the inverter. Note that for power calculation, the inverter terminal voltage, $v_{\mathrm{t},abc}$, or $v^*_{\mathrm{t},abc}$ if the inverter is not overmodulated, is used. In case $v_{\mathrm{t},abc}$ is used, as it is heavily polluted with inverter switching harmonics, the calculated real/reactive power must be filtered by a second-order filter with a relatively low cut-off frequency, e.g., 200 Hz. Then, using a cascade control structure, a power control block provides the grid frequency and $I_{\mathrm{d,ref}}$ for an inner inverter current control loop. The current control loop is identical to that of the GFMI or GFLI concept. In the following, first, a model of the system is derived, and then, based on the model, a 2×2 controller for the power control block is designed.

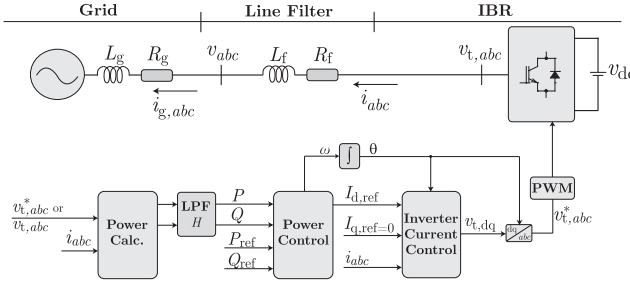

FIGURE 3. The proposed power-synchronized grid-following inverter and its control block diagrams.

A. SMALL-SIGNAL SYSTEM MODELLING

Assume a rotating reference frame aligned with the inverter current, i.e., $i_{\mathrm{q}} = 0$ A. In this dq-frame, the inverter current, $I_{\mathrm{d}}\angle 0°$, and its terminal voltage, $V_{\mathrm{t}}\angle\delta$, can be expressed as

$$i_{\mathrm{dq}} = I_{\mathrm{d}} + j0 \quad \text{and } v_{\mathrm{t,dq}} = V_{\mathrm{t}}\cos\delta + jV_{\mathrm{t}}\sin\delta. \tag{1}$$

Additionally, in every dq-frame, the inverter power is

$$P + jQ = \frac{3}{2}(v_{\mathrm{t,d}}i_{\mathrm{d}} + v_{\mathrm{t,q}}i_{\mathrm{q}} + j(v_{\mathrm{t,q}}i_{\mathrm{d}} - v_{\mathrm{t,d}}i_{\mathrm{q}})). \tag{2}$$

Replacing for i_{dq} and $v_{\mathrm{t,dq}}$ form (1) in (2), one can write

$$P + jQ = \frac{3}{2}(V_{\mathrm{t}}I_{\mathrm{d}}\cos\delta + jV_{\mathrm{t}}I_{\mathrm{d}}\sin\delta). \tag{3}$$

As shown in (3), in the dq-frame aligned with the inverter current, the real power is proportional to the d-component of

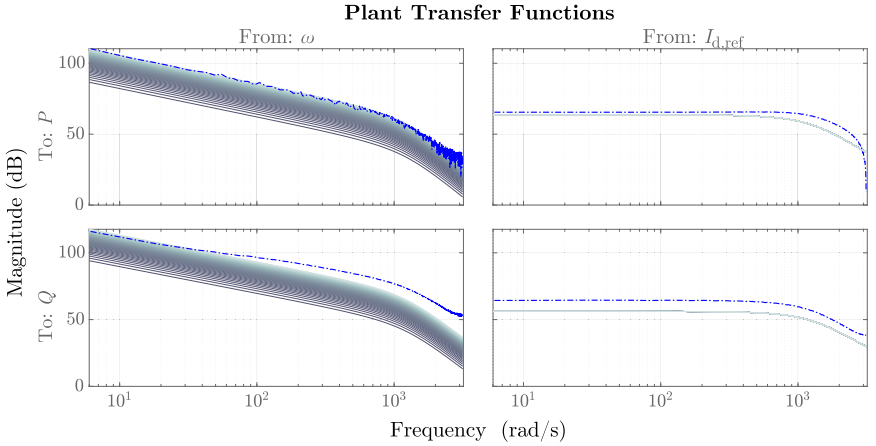

FIGURE 4. The frequency response of (5): dashed blue represents the identified system, and the shades of blue correspond to 50 parametric models with various operating points where $\delta_0 = 0.4$ rad & $I_{d,0} \in [100\ 3000]$ A. Lighter shades correspond to larger currents.

the inverter terminal voltage, while the reactive power is proportional to its q-component. Assuming a small disturbance around δ and I_d, i.e., $\delta = \delta_0 + \Delta\delta$ and $I_d = I_{d,0} + \Delta I_d$, the following dynamic model around the operating point $[\delta_0\ I_{d,0}]$ is derived:

$$\begin{bmatrix} \Delta P \\ \Delta Q \end{bmatrix} = \begin{bmatrix} -\frac{3}{2} V_t I_{d,0} \sin\delta_0 & \frac{3}{2} V_t \cos\delta_0 \\ \frac{3}{2} V_t I_{d,0} \cos\delta_0 & \frac{3}{2} V_t \sin\delta_0 \end{bmatrix} \begin{bmatrix} \Delta\delta \\ \Delta I_d \end{bmatrix}. \quad (4)$$

Assume the current controller can be approximated by a first-order delay with a delay of τ. Additionally, assume the calculated real and reactive power are filtered by a second-order low-pass filter (LPF) H with a damping factor of 0.7 and a bandwidth of 200 Hz. Then, assuming $\omega = -\frac{d\delta}{dt}$, one can write

$$\begin{bmatrix} \Delta P \\ \Delta Q \end{bmatrix} = \underbrace{\begin{bmatrix} \frac{3V_t I_{d,0} \sin\delta_0}{2s} H & \frac{3V_t \cos\delta_0}{2(1+\tau s)} H \\ -\frac{3V_t I_{d,0} \cos\delta_0}{2s} H & \frac{3V_t \sin\delta_0}{2(1+\tau s)} H \end{bmatrix}}_{\mathbf{G}} \begin{bmatrix} \Delta\omega \\ \Delta I_{d,\text{ref}} \end{bmatrix} \quad (5)$$

where $\mathbf{G}$ is the plant transfer function matrix. ω used for Park transformation represents a clockwise rotation while changes in δ are counterclockwise; hence the negative sign for deriving ω. Note that this model does not depend on the grid dynamics and its impedance as far as the vector current control is tuned such that its performance can be modeled by a first-order delay. This is achievable if fair estimates of the filter and grid impedance are available. The filter impedance can be precisely measured, and the grid impedance may be estimated via the grid short circuit ratio (SCR) and X/R ratio, which are often available at the point of connection in a power system. Additionally, several approaches for grid impedance estimation are available [38], [39].

To verify the accuracy of the model of (5), the non-parametric model (spectral model) of a simulated system with the parameters given in Table 1 is identified in Matlab/PLECS. The identification is carried out by injecting a Pseudo-Random Binary Sequence (PRBS) at the inputs of the system, i.e., ω and $I_{d,\text{ref}}$, and monitoring the system outputs, i.e., P and Q, when operating at the rated conditions. The identified model is shown in dashed blue in Fig. 4. For comparison, the frequency response of 50 parametric models are also shown in this figure with shades of blue. These 50 models have the same parameters as shown in Table 1, however, their operating points differ within the following range $I_{d,0} \in [100\ 3000]$ A, and $\delta_0 = 0.4$ rad. Lighter shades of blue correspond to larger $I_{d,0}$, while darker shades correspond to smaller $I_{d,0}$. As shown in Fig. 4, the identified nonparametric model corresponding to the rated operating point is in very close agreement with the frequency response of the parametric models with a large $I_{d,0}$. Note that variations in δ_0 also affect the system model, however, changes in δ_0 are not illustrated in Fig. 4.

TABLE 1. The parameters of the study system of Fig. 3.

Quantity	Value	Comment
L_f	100 μH	Inverter Filter Inductance
R_f	0.01 Ω	Series Resistance of L_f
L_g	770 μH	Grid Inductance
R_g	0.07 Ω	Grid Resistance
S_{base}	5 MVA	Inverter Rated Power
SCR	1.2	Grid Short Circuit Ratio (SCR) at S_{base}
v_g	690 V	Grid Line-to-Line Voltage (rms)
v_{dc}	3000 V	DC Bus Voltage
f_{sw}	5 kHz	PWM Carrier Frequency
$f_{s,id}$	2.5 kHz	PRBS Identification Sampling Frequency
f	50 Hz	System Nominal Frequency
f_{filt}	200 Hz	Power Measurement LPF Bandwidth

B. CONTROL STRUCTURE AND DESIGN

Based on the parametric model derived in the previous section for the rated conditions, one can design a 2×2 controller, which can regulate the real and reactive power exchange of

the inverter with the grid in a decoupled way. The block diagram of the controller is depicted in Fig. 5 and can be described as

$$\begin{bmatrix} \omega \\ I_{\mathrm{d,ref}} \end{bmatrix} = \underbrace{\begin{bmatrix} K_{\mathrm{PI},1} & K_{\mathrm{PI},3} \\ K_{\mathrm{PI},2} & K_{\mathrm{PI},4} \end{bmatrix}}_{\mathbf{K}} \begin{bmatrix} e_P \\ e_Q \end{bmatrix}. \tag{6}$$

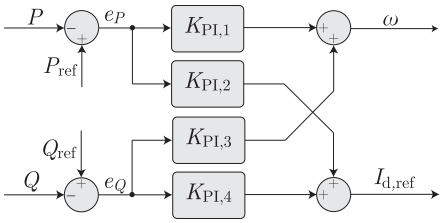

FIGURE 5. The block diagram of the proposed power controller.

This control structure consists of four PI controllers whose coefficients can be tuned using a loop-shaping-based method described in [40]. Using the frequency response of the system, this method can design fixed-order controllers (2×2 PI controllers in this case) to satisfy specific design criteria. To shape the open-loop transfer function matrix, i.e.,

$$\mathbf{L} = \mathbf{GK} = \begin{bmatrix} L_{11} & L_{12} \\ L_{21} & L_{22} \end{bmatrix}, \tag{7}$$

the square second norm of the error between the individual entries of $\mathbf{L}$ and a desired open-loop transfer function matrix, $\mathbf{L_D}$, is minimized. Consequently, the control design procedure turns into an optimization problem as follows [40]:

$$\min_{\rho} \parallel \mathbf{L}(\rho) - \mathbf{L_D} \parallel^2 \tag{8}$$

in which the vector ρ contains the coefficients of the PI controllers. The desired open-loop transfer function matrix, $\mathbf{L_D}$, is selected such that it meets certain design criteria, e.g., acceptable dynamic response and reduced coupling between the outputs, i.e., P and Q. In this paper, $\mathbf{L_D}$ is selected as

$$\mathbf{L_D} = \begin{bmatrix} L_{D1} & 0 \\ 0 & L_{D2} \end{bmatrix} = \begin{bmatrix} \dfrac{\omega_c(s+a)}{s^2} & 0 \\ 0 & \dfrac{\omega_c(s+a)}{s^2} \end{bmatrix} \tag{9}$$

in which $\omega_c = 100\frac{\mathrm{rad}}{\mathrm{s}}$ and $a = 100$. The bandwidth of the closed-loop system can be manipulated by the choice of ω_c. Note that other open-loop transfer functions could be used, however, since both the plant and the PI controllers have integrators, the open-loop transfer function must have two integrators as well. Since $\frac{\omega_c}{s^2}$ is not a stable system, a zero must be added to the desired open-loop transfer function matrix to ensure stability and provide desired dynamic performance.

The minimization problem of (8) must be subject to several constraints that shape the sensitivity function of the closed-loop system and also guarantee the stability the controller. To this end, the problem of (8) must be subject to the following linear constraints [40]:

$$\begin{aligned} &|W_1(j\omega)[1 + L_{Dq}(j\omega, \rho)]| \\ &\quad -\mathcal{R}e\{[1 + L_{Dq}(-j\omega)][1 + L_{qq}(j\omega, \rho)]\} < 0 \\ &\quad \forall\omega \in \mathbb{R} \quad \text{and } q = 1, 2 \end{aligned} \tag{10}$$

where $W_1(j\omega)$ is a weighting filter. In this paper, $W_1(j\omega) = 0.5$, which guarantees a gain margin of at least two and a phase margin of greater than 29 degrees [41]. Additionally, to ensure the stability of the closed-loop system, (8) must satisfy the generalized Nyquist stability criterion. Therefore, the minimization problem must also satisfy the following constraints [40]:

$$\begin{aligned} r_q(\omega, \rho) - \frac{\mathcal{R}e\{[1 + L_{Dq}(-j\omega)][1 + L_{qq}(j\omega, \rho)]\}}{|1 + L_{Dq}(j\omega)|} < 0 \\ \forall\omega \text{ for and } q = 1, 2, \end{aligned} \tag{11}$$

where $r_1(\omega, \rho)$ and $r_2(\omega, \rho)$ are defined as

$$r_1(\omega, \rho) = |L_{21}(j\omega, \rho)| \quad \text{and} \quad r_2(\omega, \rho) = |L_{12}(j\omega, \rho)|. \tag{12}$$

Further details about the minimization problem and the constraints can be found in [6], [40].

In this paper, taking the parametric model of (5) for the rated power conditions, i.e., when the inverter is exporting its full power when connected to a grid with parameters in Table 1, a controller is designed as follows:

$$\mathbf{K} = \begin{bmatrix} 9.063e{-}6 + \dfrac{5.59e{-}6}{s} & -2.09e{-}5 + \dfrac{-1.47e{-}4}{s} \\ 2.25e{-}6 + \dfrac{74.49e{-}3}{s} & -4.78e{-}7 + \dfrac{29.86e{-}3}{s} \end{bmatrix}. \tag{13}$$

C. CLOSED-LOOP SYSTEM STABILITY ANALYSIS

Taking this controller and the models for the aforementioned 50 operating points, the closed-loop frequency responses of the system are calculated and shown in shades of pink in Fig. 6. As the off-diagonal elements have gains well below 0 db, the designed controller results in a decoupled closed-loop system for a range of operating points. Additionally, for larger $I_{\mathrm{d},0}$ (lighter shades), the diagonal elements of the closed-loop system have a bandwidth of around 100 $\frac{\mathrm{rad}}{s}$, which is in agreement with the predicted bandwidth of the open-loop transfer function of (9). However, for smaller $I_{\mathrm{d},0}$ (darker shades), the bandwidth of the reactive power control reduces, although the real power control bandwidth and decoupling do not experience significant changes. To have fixed bandwidth over a broad range of inverter currents, one can use gain-scheduled controllers with the inverter current as the scheduling parameter. Note that one can also use the identified nonparametric frequency response of the system to design the controller, and the designed controller should exhibit similar performance to the controller of (13).

Additionally, to analyze the robustness of the designed controller with respect to inverter current variations, the poles of the closed-loop system when the inverter current, i.e., $I_{\mathrm{d},0}$,

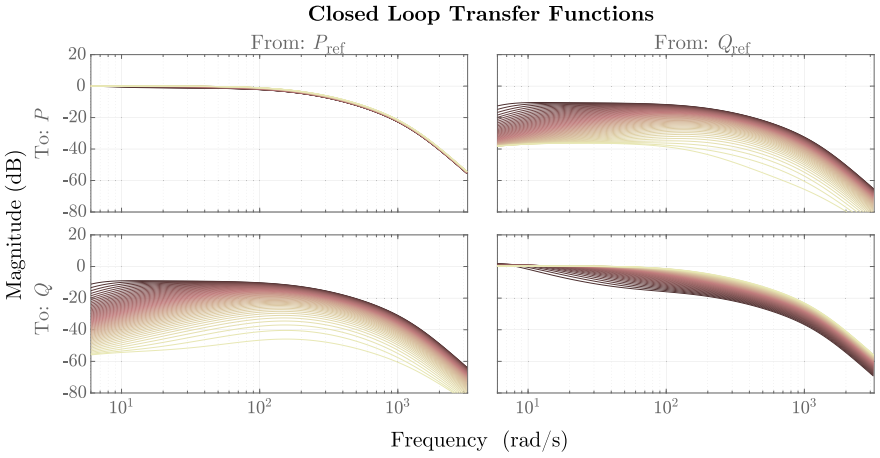

FIGURE 6. The frequency response of the closed-loop system for 50 parametric models with various operating points where $\delta_0 = 0.4$ rad & $I_{d,0} \in [100\ 3000]$ A. Lighter shades correspond to larger currents.

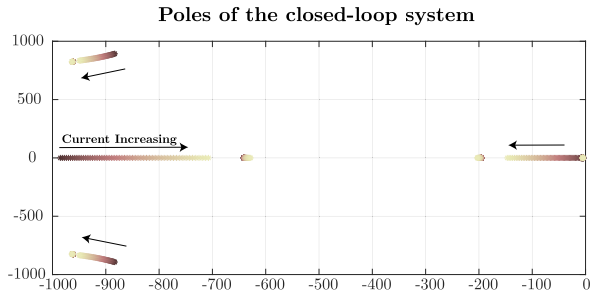

FIGURE 7. The closed-loop system poles operating with the controller of (13) for 50 operating points where $\delta_0 = 0.4$ rad & $I_{d,0} \in [100\ 3000]$ A. Lighter shades correspond to larger currents.

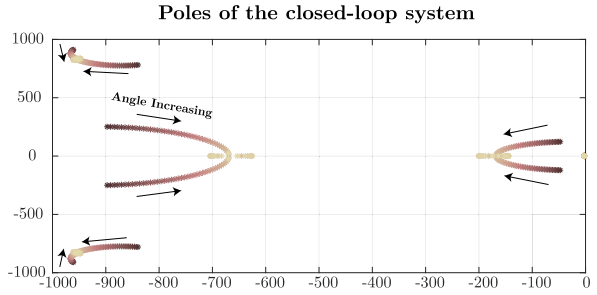

FIGURE 8. The closed-loop system poles operating with the controller of (13) for 75 operating points where $\delta_0 \in [-0.4\ 0.4]$ rad & $I_{d,0} = 3000$ A. Lighter shades correspond to larger angles.

changes from its nominal value (3000 A) to a very low value (100 A), are depicted in Fig. 7. Moreover, the same analysis is carried out when the phase angle of the inverter terminal voltage, i.e., δ_0, changes from -0.4 rad to 0.4 rad, and the closed-loop system poles are shown in Fig. 8. For all of these operating points, the poles of the closed-loop system are on the left-hand side of the imaginary axis. These analyses confirm the designed controller is robust with respect the variations in the inverter power set-points and maintains the system stability for various operating points.

IV. PERFORMANCE EVALUATION

To evaluate the performance of the proposed control strategy, the system of Fig. 3 is simulated in Matlab/PLECS. Additionally, a scaled-down setup, shown in Fig. 9, is implemented using a Regatron grid simulator and an Imperix inverter controlled by a BoomBox Imperix Controller. The Imperix inverter is a SiC-based two-level three-phase inverter. Also, the Boombox controller is a fully programmable control platform, including both DSP and FPGA, that can be programmed using either C or directly from Matlab/Simulink. For the simulation tests, two sets of tests (real/reactive power set-point changes and grid frequency/phase changes) are conducted for a very weak and a very stiff grid, and the performance of the proposed control strategy is contrasted with that of the VMDPC [33], [34], which is a PLL-less GFLI. Additionally, in the experimental tests, the performance of the proposed controller upon power set-point changes and grid voltage changes is evaluated.

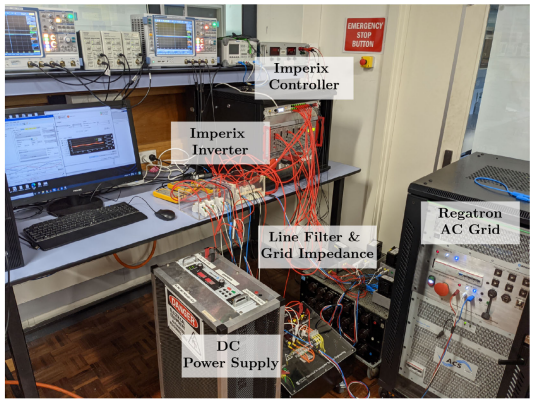

FIGURE 9. The experimental setup.

A. SIMULATION RESULTS

1) STIFF GRID WITH SCR OF 48

Assuming the parameters of Table 1 and the designed controller of (13), the performance of the proposed control strategy is evaluated for a very strong grid (SCR = 48). To achieve this SCR, the grid inductance/resistance are selected as 17.5 μH and 0.0017 Ω, respectively. Note that as the PoC voltage is not required for the proposed approach, there is no upper bound for the SCR at which the controller remains stable. The reason is that from the controller's point of view, a filter inductance of 100 μH plus a grid inductance of 17.5 μH is not different from a filter inductance of 115 μH plus a grid inductance of 2.5 μH, where the second scenario results in an SCR of 336.

The inverter is initially operating in a steady-state and injects $P = 1$ MW and $Q = 0$ MVAR. At $t = 0.1$ s ($t = 0.25$ s), the real power (the reactive power) set-point steps up to 4 MW (2 MVAR). Additionally, at $t = 0.4$ s, the power factor of the inverter is changed from 0.9 to 0.45. Fig. 10 shows the results of the conducted test for this stiff grid. The three-phase PoC voltage and the inverter current are depicted in Fig. 10(a) and 10(b), respectively. The dq-components of the inverter terminal voltage reference and the dq-components of the inverter's current are shown in Fig. 10(c) and 10(d), respectively. The dq-components of the inverter terminal voltage reference change such that the q-component component of the inverter current is regulated at zero while its d-component varies to ensure the real/reactive power set-points are tracked with zero steady-state error. Additionally, as shown in Fig. 10(e), the controller tracks the grid frequency such that the reference frame in which the controller operates is synchronized with the grid. The real/reactive power of the inverter are shown in Fig. 10(f), and as predicted, the controller tracks the changes with zero steady-state error in around 10 ms.

To test the impact of the grid voltage frequency and phase changes on the controller, the frequency of the grid voltage is changed to 50.25 Hz at $t = 0.6$ s. This change is applied such that it results in a phase jump of 20°. The inverter initially injects 2 MW of real power and 4 MVAR of reactive power. As shown in Fig. 11, the controller can maintain the stability of the system upon this change in the system and successfully rejects this severe disturbance. The three-phase PoC voltage and inverter current are shown in

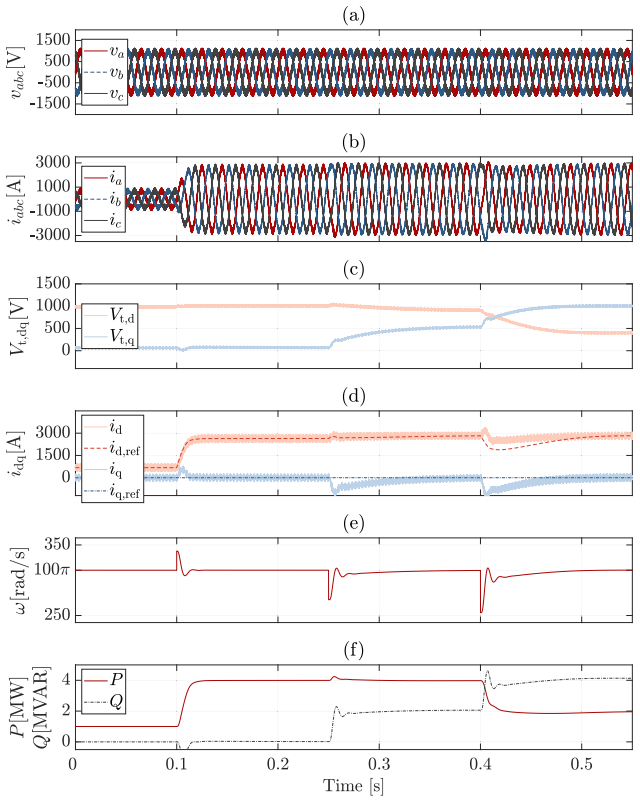

FIGURE 10. The simulation results of the system of Fig. 3 operating in a very strong grid when subjected to changes in its real/reactive power set-points: (a) the three-phase PoC voltage, (b) the three-phase inverter currents, (c) the dq-components of the inverter terminal voltage reference, (d) the dq-components of the inverter current and their references, (e) the system frequency extracted by the controller, and (f) the real/reactive power of the inverter.

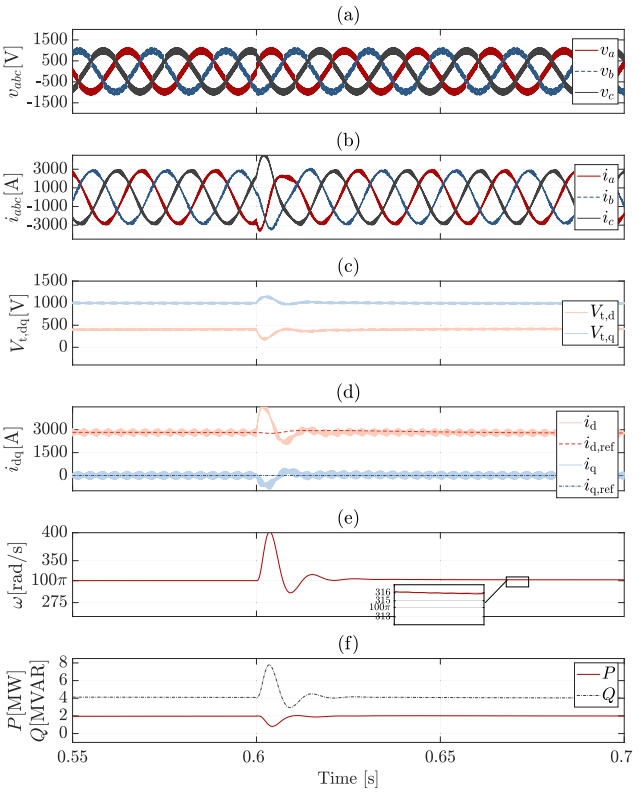

FIGURE 11. The simulation results of the system of Fig. 3 operating in a very strong grid when subjected to a grid frequency change: (a) the three-phase PoC voltage, (b) the three-phase inverter currents, (c) the dq-components of the inverter terminal voltage reference, (d) the dq-components of the inverter current and their references, (e) the system frequency extracted by the controller, and (f) the real/reactive power of the inverter.

Fig. 11(a) and 11(b), respectively. The dq-components of the inverter terminal voltage reference and the dq-components of the inverter current are also depicted in Fig. 11(c) and 11(d), respectively. The grid frequency extracted by the control strategy is shown in Fig. 11(e), which undergoes a significant change upon the step-change in the grid frequency, however, the controller is able to successfully track the change. Finally, the real/reactive power of the inverter are shown in Fig. 11(f), which upon the step-change experience a transient and are eventually controlled at their references.

To contrast the performance of the proposed controller with an existing controller, the same tests are applied to the VMDPC strategy operating in a system with parameters given in Table 1. The block diagram of the VMDPC is depicted in Fig. 12. Unlike the proposed controller in this paper, the VMDPC requires the PoC voltage for its operation, which deteriorates its performance in week grids. The VMDPC parameters are tuned according to the procedure described in [32], [34]. The same real/reactive power set-point change and grid frequency change are applied, and the results are reported in Fig. 13 and Fig. 14, respectively. The VMDPC can track the power set-points in a reasonable amount of time, however, the real and reactive power experience significant oscillation upon every change. To damp these oscillations, one can reduce the proportional gain of the PI controllers used in the VMDPC, however, this reduces the bandwidth of the controller and results in slower dynamics.

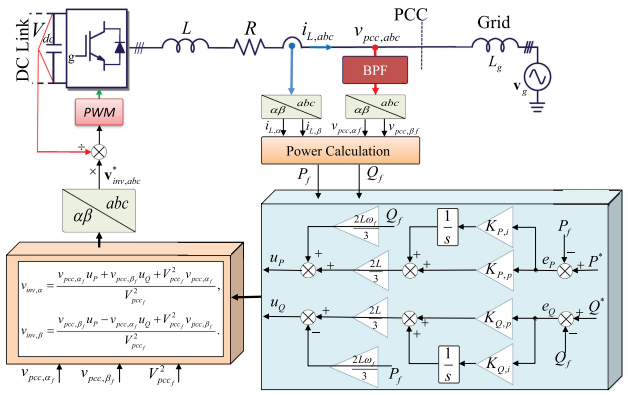

FIGURE 12. A grid-following inverter and its control block diagram controlled by the VMDPC for weak grids [34]. For further details and the definition of the parameters and variables used in this block diagram, refer to [34].

2) WEAK GRID WITH SCR OF 1.2

To evaluate the performance of the proposed controller in a weak grid, the SCR of the system simulated in the previous test is decreased to 1.2, i.e., the grid impedance is increased 40 times, while other parameters are identical to those of the previous test, and a similar test pattern is applied to the set-points. Fig. 15 shows the results of the conducted test for this weak grid and confirms the performance of the controller is very similar to that of a strong grid. The inverter three-phase PoC voltage and current are shown in Fig. 15(a) and 15(b),

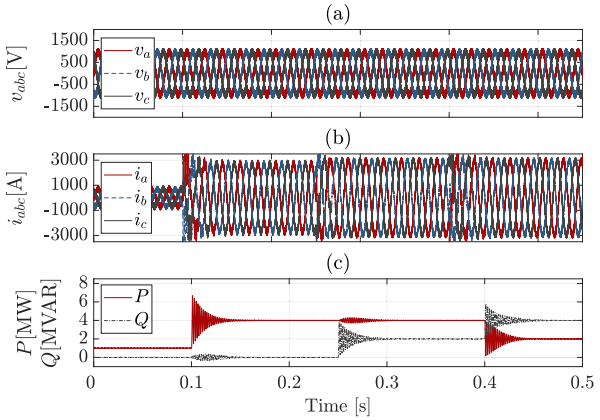

FIGURE 13. The simulation results of VMDPC [33], [34] operating in a very strong grid when subjected to changes in its real/reactive power set-points: (a) the three-phase PoC voltage, (b) the three-phase inverter current, and (c) the real/reactive power of the inverter.

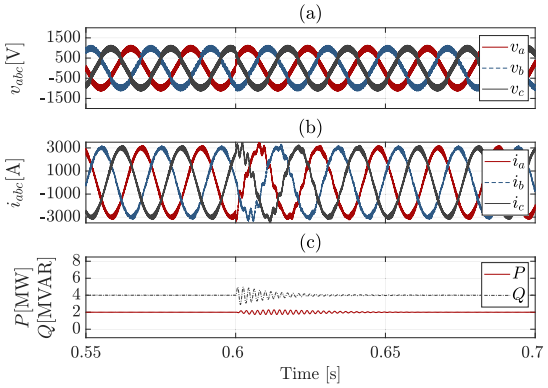

FIGURE 14. The simulation results of VMDPC [33], [34] operating in a very strong grid when subjected to a grid frequency change: (a) the three-phase PoC voltage, (b) the three-phase inverter current, and (c) the real/reactive power of the inverter.

respectively. Compared to the previous test, the PoC voltage contains more harmonics. The main reason is that the grid impedance in the stiff grid case is much lower; hence, the PoC is electrically closer to the grid. However, since the overall inductance between the inverter and the grid is higher in the weak grid case, the harmonic content of the inverter current is less in this case. The dq-components of the inverter terminal voltage reference and the dq-components of the inverter current are illustrated in Fig. 15(c) and 15(d), respectively. Additionally, the grid frequency extracted by the controller is shown in Fig. 15(e). It can be seen that upon each change, the dq-components of the inverter terminal voltage reference change such that the q-component of the inverter current is regulated at zero while the d-component of the inverter current changes to meet the inverter power injection set-points. The system frequency is also extracted by the controller such that the dq-frame of the control strategy is synchronized with the grid in the steady-state. Finally, the real and reactive power of the inverter are depicted in Fig. 15(f). The controller

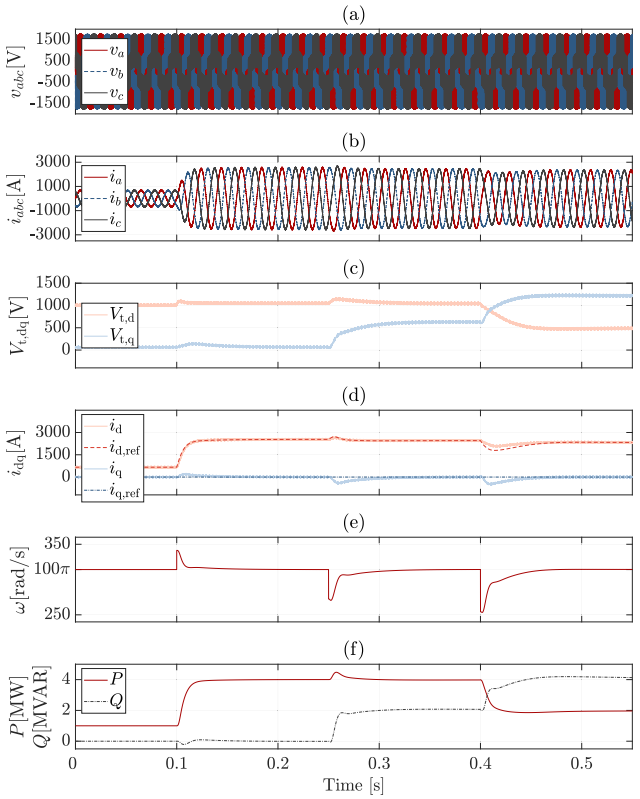

FIGURE 15. The simulation results of the system of Fig. 3 operating in a very weak grid when subjected to changes in its real/reactive power set-points: (a) the three-phase PoC voltage, (b) the three-phase inverter currents, (c) the dq-components of the inverter terminal voltage reference, (d) the dq-components of the inverter current and their references, (e) the system frequency extracted by the controller, and (f) the real/reactive power of the inverter.

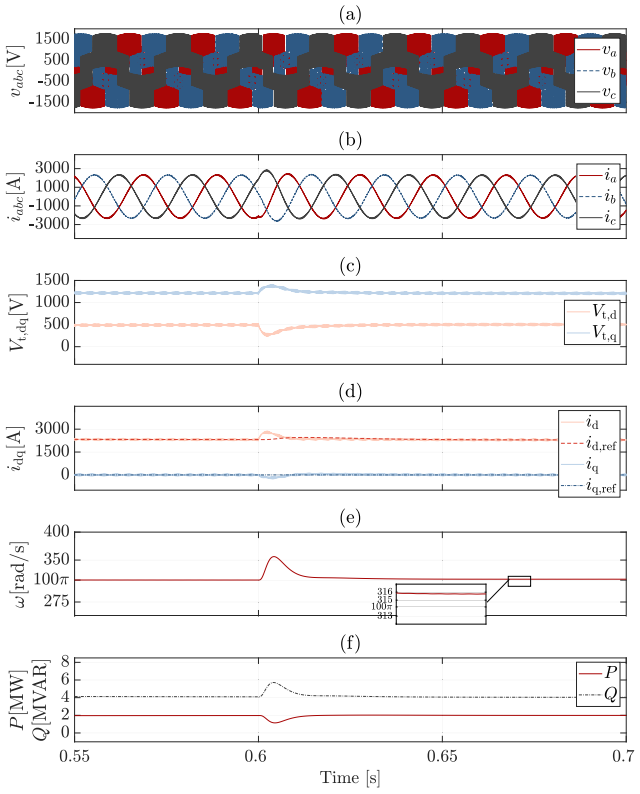

FIGURE 16. The simulation results of the system of Fig. 3 operating in a very weak grid when subjected to a grid frequency change: (a) the three-phase PoC voltage, (b) the three-phase inverter currents, (c) the dq-components of the inverter terminal voltage reference, (d) the dq-components of the inverter current and their references, (e) the system frequency extracted by the controller, and (f) the real/reactive power of the inverter.

can track changes in the power set-points in around 10 ms, while the impact of the real power (reactive power) change on the reactive power (real power) is negligible, which confirms the decoupling effect of the controller.

To evaluate the impact of the grid voltage frequency changes and phase jumps on the controller, the frequency of the grid voltage is changed to 50.25 Hz at $t = 0.6$ s. Similar to the previous test, this change is applied such that it results in a phase jump of 20°. The inverter initially injects 2 MW of real power and 4 MVAR of reactive power. As shown in Fig. 16, the controller can maintain the stability of the system upon this change in the system and successfully rejects this severe disturbance. The three-phase PoC voltage and inverter current are shown in Fig. 16(a) and 16(b), respectively. The dq-components of the inverter terminal voltage reference and the dq-components of the inverter current are also depicted in Fig. 16(c) and 16(d), respectively. The grid frequency extracted by the control strategy is shown in Fig. 16(e), which undergoes a significant change upon the step-change in the grid frequency, however, the controller is able to successfully track the change. Finally, the real/reactive power of the inverter are shown in Fig. 16(f), which upon the step-change experience a transient and are eventually regulated at their references. As the inverter is electrically further from the grid, the post-disturbance waveforms undergo a less severe transient compared to the strong grid case.

To contrast the performance of the proposed controller in a weak grid with the VMDPC, the same tests are applied to the VMDPC strategy operating in a system with parameters given in Table 1. Tuning the VMDPC parameters according to the procedure described in [32] results in an unstable system for the parameters given in Table 1 when operating in a very weak grid. Therefore, the proportional gains of the PI controllers of the VMDPC are decreased such that the system is stable upon changes. This results in very slow dynamics upon various contingencies. The same real/reactive power set-point change and grid frequency change are applied, and the results are reported in Fig. 17. Since the dynamic response of the VMDPC is very slow in the weak grid, the time sequence of the tests are prolonged in this case to allow the VMDPC to reach steady-state after each test. The PQ steps are applied at $t = 0.4$ s and $t = 1.3$ s, while the power factor is changed at $t = 2.2$ s, and the grid frequency change is applied at

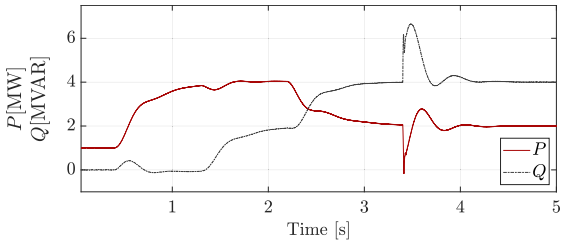

FIGURE 17. The simulation results (the real/reactive power) of the VMDPC [33], [34] operating in a very weak grid when subjected to changes in its real/reactive power set-points and a grid frequency change.

$t = 3.4\ s$. Also, due to the prolonged time, only the DC values, i.e., real/reactive power, are shown.

As shown in Fig. 17, although the VMDPC tracks the power set-points and rejects the frequency change disturbance, upon every change, the real/reactive power reach steady-state in more than 1 s. For the proposed controller, however, the results for the stiff grid are in very close agreement with those of the weak grid, although there are slight differences between the two cases immediately after a contingency. Note that the only difference in the proposed control strategy for the weak and strong grid cases is the internal current controller, which is tuned according to the grid impedance for each case.

B. EXPERIMENTAL RESULTS

In this section, adopting the experimental setup shown in Fig. 9, the performance of the proposed control strategy is evaluated in a scaled-down setup whose parameters are shown in Table 2. The performance of the controller is evaluated for both strong and weak grids. To conduct the experiments, two test scenarios are adopted: 1) grid-related scenarios in which a voltage sag, a voltage imbalance, and a voltage phase jump (each for 0.2 s) are applied for strong and weak grids, and 2) the real power reference changes for strong and weak grids.

TABLE 2. The parameters of the experimental setup.

Quantity	Value	Comment
L_g	14 mH	Grid Inductance for Weak Grid (SCR=0.9)
L_g	2 mH	Grid Inductance for Strong Grid (SCR=6.4)
L_f	2 mH	Filter Inductance
R_g	1.1 Ω	Grid Resistance for Weak Grid
R_g	0.3 Ω	Grid Resistance for Strong Grid
R_f	0.2 Ω	Filter Resistance
S_{base}	2500 VA	Inverter Rated Power
v_g	100 V	Grid Line-to-Line Voltage Amplitude
v_{dc}	350 V	DC Bus Voltage
f_{sw}	20 kHz	PWM Carrier Frequency
f	50 Hz	System Nominal Frequency
f_{filt}	200 Hz	Power Measurement LPF Bandwidth

Note that to avoid excessive transients upon inverter startup, one can start the inverter with the power controller inactive and set ω to its rated value, i.e., $2\pi 50$ rad/s, and $I_{d,ref} = 0$ A. Then, after the initial transients settle down, setting $P_{ref} = 0$ W and $Q_{ref} = 0$ VAR, the two PI-controllers responsible for generating ω can be started to get synchronized with the grid. After the transients for this step are settled down, the PI controllers responsible for $I_{d,ref}$ can be started. This procedure results in a smooth startup and is adopted in the experimental tests.

1) GRID VOLTAGE-RELATED SCENARIOS

The experimental setup of Fig. 9 initially operates in the steady-state, and injects $P = 1200$ W and $Q = 900$ VAR to the grid. The filter/impedance value corresponding to a strong grid (see Table 2) is utilized that results in an SCR of 6.4. At $t = 0.1$ s, the grid voltage experiences a voltage sag, and its amplitude drops to 0.75 pu. Subsequently, at $t = 0.3$ s, the voltage is restored, however, 10% of voltage imbalance is applied to the grid voltage. Finally, at $t = 0.5$ s, the imbalance is removed, however, a phase jump of 15° is applied.

Fig. 18(a) and 18(b) show the three-phase grid voltage and inverter terminal voltage reference, respectively. As only one inductor is used to represent the combined inverter filter and the grid impedance, the PoC voltage is not shown.

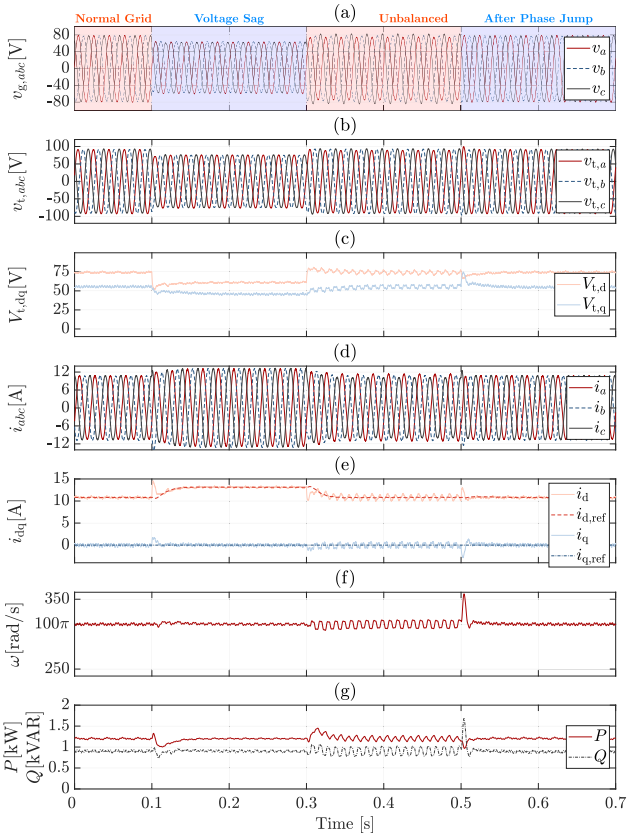

FIGURE 18. The experimental results of the system of Fig. 3 operating in a strong grid with an SCR of 6.4 when the grid voltage amplitude drops, the grid voltage becomes unbalanced, and the grid voltage phase angle jumps for 15°: (a) the three-phase grid voltage, (b) the three-phase inverter terminal voltage reference, (c) the dq-components of the inverter terminal voltage reference, (d) the three-phase inverter current and their references, (e) the dq-components of the inverter current and their references, (f) the system frequency extracted by the controller, and (g) the inverter's real/reactive power.

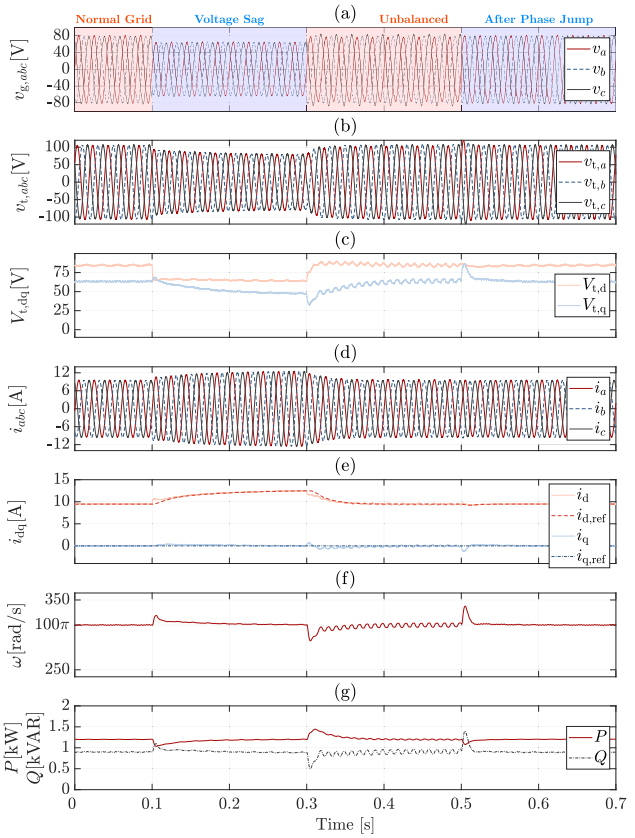

FIGURE 19. The experimental results of the system of Fig. 3 operating in a weak grid with an SCR of 0.9 when the grid voltage amplitude drops, the grid voltage becomes unbalanced, and the grid voltage phase angle jumps for 15°: (a) the three-phase grid voltage, (b) the three-phase inverter terminal voltage reference, (c) the dq-components of the inverter terminal voltage reference, (d) the three-phase inverter current and their references, (e) the dq-components of the inverter current and their references, (f) the system frequency extracted by the controller, and (g) the inverter's real/reactive power.

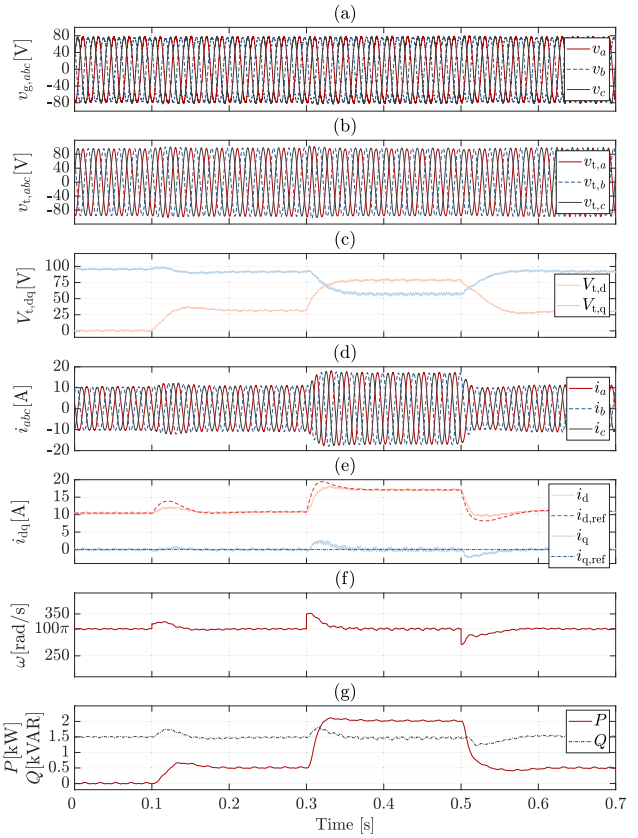

FIGURE 20. The experimental results of the system of Fig. 3 operating in a strong grid with an SCR of 6.4 when the real power set-point steps up and down: (a) the three-phase grid voltage, (b) the three-phase inverter terminal voltage reference, (c) the dq-components of the inverter terminal voltage reference, (d) the three-phase inverter current and their references, (e) the dq-components of the inverter current and their references, (f) the system frequency extracted by the controller, and (g) the inverter's real/reactive power.

Fig. 18(c) depicts the dq-components of the inverter terminal voltage reference. The three-phase inverter current and their dq-components are shown in Fig. 18(d) and 18(e), respectively. The grid frequency extracted by the controller is shown in Fig. 18(f), which confirms the controller ability to track frequency changes and maintain the system's stability upon various contingencies. Additionally, the real/reactive power are illustrated in Fig. 18(g), which confirm the inverter ability to reject disturbances in around 10 ms. It must be noted that the waveforms shown for experimental tests do not contain any switching harmonic as their sampling frequency is equal to the switching frequency.

For the weak grid, the grid inductance (resistance) is increased to 14 mH (1.1 Ω), which corresponds to an SCR of 0.9. The same test sequence as the strong grid is applied to the grid voltage in this weak grid, and the results are reported Fig. 19, which are the dual of those reported in Fig. 18. Contrasting the results in these figures confirms that the controller can seamlessly perform in both weak and strong grids and maintain its stability.

2) POWER SET-POINT CHANGES

To evaluate the performance of the controller when subjected to changes in the power set-points, the experimental platform of Fig. 9 is first configured such that it represents a strong grid with an SCR of 6.4, i.e., the grid inductance is 2 mH. The setup initially operates in the steady-state and injects $P = 0$ W and $Q = 1500$ VAR to the grid. At $t = 0.1$ s and $t = 0.3$ s, the real power set-points steps up to 500 W and 1500 W, respectively, and finally, at $t = 0.5$ s, it steps down to 500 W again.

Fig. 20(a) and 20(b) show the three-phase grid voltage and inverter terminal voltage reference, respectively. As only one inductor is used to represent the combined inverter filter and the grid impedance, the PoC voltage is not shown. Fig. 20(c) depicts the dq-components of the inverter terminal voltage reference. The three-phase inverter current and their dq-components are shown in Fig. 20(d) and 20(e), respectively. The grid frequency extracted by the controller is shown in Fig. 20(f), which confirms the controller ability to track frequency changes and maintain the system's stability upon

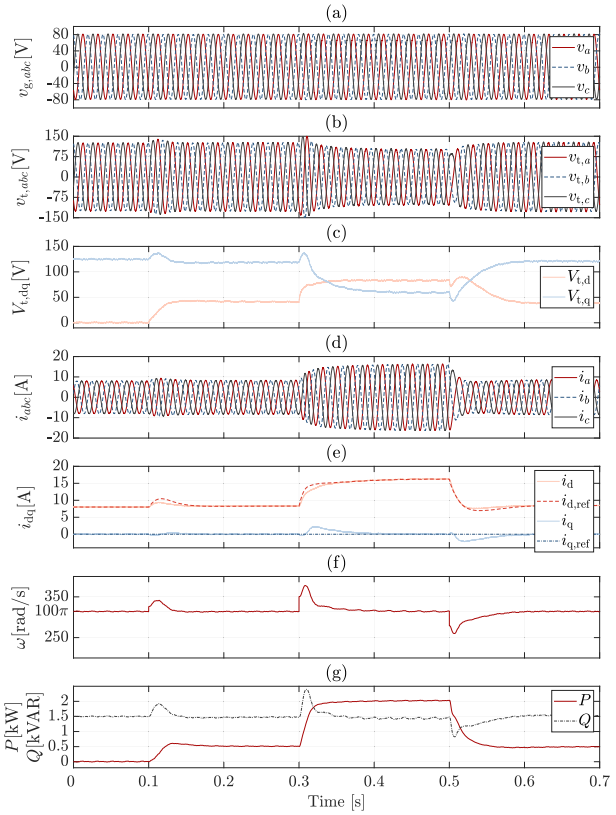

FIGURE 21. The experimental results of the system of Fig. 3 operating in a weak grid with an SCR of 0.9 when the real power set-point steps up and down: (a) the three-phase grid voltage, (b) the three-phase inverter terminal voltage reference, (c) the dq-components of the inverter terminal voltage reference, (d) the three-phase inverter current and their references, (e) the dq-components of the inverter current and their references, (f) the system frequency extracted by the controller, and (g) the inverter's real/reactive power.

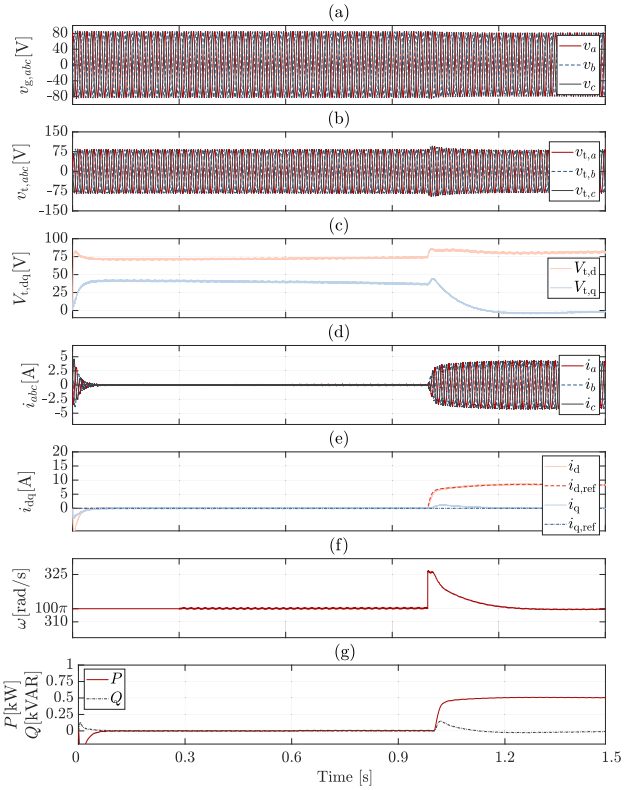

FIGURE 22. The experimental results of the system operating in a weak grid upon startup and subsequently a step-up change in the real power set-point: (a) the three-phase grid voltage, (b) the three-phase inverter terminal voltage reference, (c) the dq-components of the inverter terminal voltage reference, (d) the three-phase inverter current and their references, (e) the dq-components of the inverter current and their references, (f) the system frequency extracted by the controller, and (g) the inverter's real/reactive power.

real power set-point changes. Additionally, the real/reactive power are illustrated in Fig. 20(g), which confirm the ability of the inverter in tracking the set-point changes in around 10 ms in a decoupled way.

Similar to the previous test, for the weak grid, the grid inductance (resistance) is increased to 14 mH (1.1 Ω), which corresponds to an SCR of 0.9. The same set-point change sequence as the strong grid is applied to the real power in this weak grid, and the results are reported Fig. 21, which are the dual of those reported in Fig. 20. Contrasting the results in these figures confirms the controller can seamlessly perform in both weak and strong grids and maintain its stability.

3) INVERTER STARTUP

To start the inverter, one can start with the power controller inactive, and set ω to its rated value, i.e., $2\pi 50$ rad/s, and $I_{\mathrm{d,ref}} = 0$ A. Then, after the initial transients settle down, setting $P_{\mathrm{ref}} = 0$ W and $Q_{\mathrm{ref}} = 0$ VAR, the two PI-controllers responsible for generating ω can be started (at $t = 0.3$ s in Fig. 22) to get synchronized with the grid. Then, after the transients for this step are settled down, the PI controllers responsible for $I_{\mathrm{d,ref}}$ can be started (at $t = 0.6$ s in Fig. 22). This procedure results in a smooth startup. In Fig. 22, the experimental results for the inverter startup for the weak grid are shown in which the inverter starts, and after 1 s, the real power set-point is stepped up to 500 W. The strong grid startup is very similar to the weak grid and not shown here.

V. CONCLUSION

This paper proposes a power-synchronized control strategy for grid-following inverters that contrary to the existing solutions for grid-following inverters does not require any PLL or PoC voltage sensing for its operation. Hence, the proposed controller can seamlessly operate in ultra-weak grids. Additionally, as opposed to grid-forming inverters, as the proposed approach does not rely on voltage regulation at the PoC, it can reliably operate in stiff and/or series-compensated grids as well. While no PoC voltage sensing/regulation is needed, the proposed controller utilizes the inverter terminal voltage and its current to control the real and reactive power exchange with the grid in a decoupled way. Moreover,

the dynamic performance of the proposed controller can be effortlessly tuned via the choice of a desired open-loop transfer function. From a hardware point of view, the proposed approach is identical to existing grid-following inverters; hence, it can be easily retrofitted into the existing large fleet of grid-following inverters to enhance their performance in weak grids.

ACKNOWLEDGMENT

The assistance provided by Mr. Dayan Rathnayake and Mr. Si Phu Me with the experiments is greatly appreciated.

REFERENCES

[1] J. A. Suul, S. D'Arco, P. Rodríguez, and M. Molinas, "Impedance-compensated grid synchronisation for extending the stability range of weak grids with voltage source converters," *IET Gen. Transmiss. Distrib.*, vol. 10, no. 6, pp. 1315–1326, Apr. 2016.

[2] R. Teodorescu, M. Liserre, and P. Rodriguez, *Grid Converters for Photovoltaic and Wind Power Systems*. Hoboken, NJ, USA: Wiley, 2010.

[3] J. Rocabert, A. Luna, F. Blaabjerg, and P. Rodríguez, "Control of power converters in AC microgrids," *IEEE Trans. Power Electron.*, vol. 27, no. 11, pp. 4734–4749, Nov. 2012.

[4] S. Golestan, J. M. Guerrero, J. C. Vasquez, A. M. Abusorrah, and Y. Al-Turki, "All-pass-filter-based PLL systems: Linear modeling, analysis, and comparative evaluation," *IEEE Trans. Power Electron.*, vol. 35, no. 4, pp. 3558–3572, Aug. 2020.

[5] B. Bahrani, S. Kenzelmann, and A. Rufer, "Multivariable-PI-based *dq* current control of voltage source converters with superior axis decoupling capability," *IEEE Trans. Ind. Electron.*, vol. 58, no. 7, pp. 3016–3026, Aug. 2011.

[6] B. Bahrani, M. Vasiladiotis, and A. Rufer, "High-order vector control of grid-connected voltage-source converters with LCL-filters," *IEEE Trans. Ind. Electron.*, vol. 61, no. 6, pp. 2767–2775, Jun. 2014.

[7] B. Bahrani, "Advanced control strategies for voltage source converters in microgrids and traction networks," Ph.D. dissertation, École polytechnique fédérale de Lausanne, Lausanne, Switzerland, 2012.

[8] R. H. Lasseter, Z. Chen, and D. Pattabiraman, "Grid-forming inverters: A critical asset for the power grid," *IEEE J. Emerg. Sel. Topics Power Electron.*, vol. 8, no. 2, pp. 925–935, Jun. 2020.

[9] L. Zhang, L. Harnefors, and H.-P. Nee, "Power-synchronization control of grid-connected voltage-source converters," *IEEE Trans. Power Syst.*, vol. 25, no. 2, pp. 809–820, May 2010.

[10] X. Meng, J. Liu, and Z. Liu, "A generalized droop control for grid-supporting inverter based on comparison between traditional droop control and virtual synchronous generator control," *IEEE Trans. Power Electron.*, vol. 34, no. 6, pp. 5416–5438, Jun. 2019.

[11] Q.-C. Zhong and G. Weiss, "Synchronverters: Inverters that mimic synchronous generators," *IEEE Trans. Ind. Electron.*, vol. 58, no. 4, pp. 1259–1267, Apr. 2011.

[12] M. Yazdanian and A. Mehrizi-Sani, "Washout filter-based power sharing," *IEEE Trans. Smart Grid*, vol. 7, no. 2, pp. 967–968, Mar. 2016.

[13] X. Wang, M. G. Taul, H. Wu, Y. Liao, F. Blaabjerg, and L. Harnefors, "Grid-synchronization stability of converter-based resources—An overview," *IEEE Open J. Ind. Appl.*, vol. 1, pp. 115–134, 2020.

[14] J. Z. Zhou, H. Ding, S. Fan, Y. Zhang, and A. M. Gole, "Impact of short-circuit ratio and phase-locked-loop parameters on the small-signal behavior of a VSC-HVDC converter," *IEEE Trans. Power Del.*, vol. 29, no. 5, pp. 2287–2296, Oct. 2014.

[15] D. Yang and X. Wang, "Unified modular state-space modeling of grid-connected voltage-source converters," *IEEE Trans. Power Electron.*, vol. 35, no. 9, pp. 9700–9715, Sep. 2020.

[16] M. Z. Mansour, S. P. Me, S. Hadavi, B. Badrazadeh, A. Karimi, and B. Bahrani, "Nonlinear transient stability analysis of phased-locked loop based grid-following voltage source converters using Lyapunov's direct method," *IEEE J. Emerg. Sel. Topics Power Electron.*, early access, Feb. 8, 2021, doi: 10.1109/JESTPE.2021.3057639.

[17] D. Yang, X. Wang, F. Liu, K. Xin, Y. Liu, and F. Blaabjerg, "Symmetrical PLL for SISO impedance modeling and enhanced stability in weak grids," *IEEE Trans. Power Electron.*, vol. 35, no. 2, pp. 1473–1483, Feb. 2020.

[18] J. Fang, X. Li, H. Li, and Y. Tang, "Stability improvement for three-phase grid-connected converters through impedance reshaping in quadrature-axis," *IEEE Trans. Power Electron.*, vol. 33, no. 10, pp. 8365–8375, Oct. 2018.

[19] K. M. Alawasa, Y. A.-R. I. Mohamed, and W. Xu, "Active mitigation of subsynchronous interactions between PWM voltage-source converters and power networks," *IEEE Trans. Power Electron.*, vol. 29, no. 1, pp. 121–134, Jan. 2014.

[20] X. Zhang, S. Fu, W. Chen, N. Zhao, G. Wang, and D. Xu, "A symmetrical control method for grid-connected converters to suppress the frequency coupling under weak grid conditions," *IEEE Trans. Power Electron.*, vol. 35, no. 12, pp. 13488–13499, Apr. 2020.

[21] Y. Liao, X. Wang, F. Liu, K. Xin, and Y. Liu, "Sub-synchronous control interaction in grid-forming VSCs with droop control," in *Proc. 4th IEEE Workshop Electron. Grid (eGRID)*, Nov. 2019, pp. 1–6.

[22] S. Wang, Z. Liu, J. Liu, D. Boroyevich, and R. Burgos, "Small-signal modeling and stability prediction of parallel droop-controlled inverters based on terminal characteristics of individual inverters," *IEEE Trans. Power Electron.*, vol. 35, no. 1, pp. 1045–1063, Jan. 2020.

[23] M. M. Esfahani, H. F. Habib, and O. A. Mohammed, "Microgrid stability improvement using a fuzzy-based PSS design for virtual synchronous generator," in *Proc. SoutheastCon*, 2018, pp. 1–5.

[24] G. N. Baltas, N. B. Lai, L. Marin, A. Tarrasó, and P. Rodriguez, "Grid-forming power converters tuned through artificial intelligence to damp subsynchronous interactions in electrical grids," *IEEE Access*, vol. 8, pp. 93369–93379, 2020.

[25] G. Li, Y. Chen, A. Luo, Z. He, H. Wang, Z. Zhu, W. Wu, and L. Zhou, "Analysis and mitigation of subsynchronous resonance in series-compensated grid-connected system controlled by a virtual synchronous generator," *IEEE Trans. Power Electron.*, vol. 35, no. 10, pp. 11096–11107, Oct. 2020.

[26] M. G. Taul, X. Wang, P. Davari, and F. Blaabjerg, "Current limiting control with enhanced dynamics of grid-forming converters during fault conditions," *IEEE J. Emerg. Sel. Topics Power Electron.*, vol. 8, no. 2, pp. 1062–1073, Jun. 2020.

[27] M. Malinowski, M. Jasinski, and M. P. Kazmierkowski, "Simple direct power control of three-phase PWM rectifier using space-vector modulation (DPC-SVM)," *IEEE Trans. Ind. Electron.*, vol. 51, no. 2, pp. 447–454, Apr. 2004.

[28] A. Bouafia, J.-P. Gaubert, and F. Krim, "Predictive direct power control of three-phase pulsewidth modulation (PWM) rectifier using space-vector modulation (SVM)," *IEEE Trans. Power Electron.*, vol. 25, no. 1, pp. 228–236, Jan. 2010.

[29] S. Vazquez, J. A. Sanchez, J. M. Carrasco, J. I. Leon, and E. Galvan, "A model-based direct power control for three-phase power converters," *IEEE Trans. Ind. Electron.*, vol. 55, no. 4, pp. 1647–1657, Apr. 2008.

[30] D.-K. Choi and K.-B. Lee, "Dynamic performance improvement of AC/DC converter using model predictive direct power control with finite control set," *IEEE Trans. Ind. Electron.*, vol. 62, no. 2, pp. 757–767, Feb. 2015.

[31] S. Vazquez, A. Marquez, R. Aguilera, D. Quevedo, J. I. Leon, and L. G. Franquelo, "Predictive optimal switching sequence direct power control for grid-connected power converters," *IEEE Trans. Trans. Ind. Electron.*, vol. 62, no. 4, pp. 2010–2020, Mar. 2015.

[32] Y. Gui, X. Wang, F. Blaabjerg, and D. Pan, "Control of grid-connected voltage-source converters: The relationship between direct-power control and vector-current control," *IEEE Ind. Electron. Mag.*, vol. 13, no. 2, pp. 31–40, Jun. 2019.

[33] Y. Gui, X. Wang, and F. Blaabjerg, "Vector current control derived from direct power control for grid-connected inverters," *IEEE Trans. Power Electron.*, vol. 34, no. 9, pp. 9224–9235, Sep. 2019.
[34] Y. Gui, X. Wang, H. Wu, and F. Blaabjerg, "Voltage-modulated direct power control for a weak grid-connected voltage source inverters," *IEEE Trans. Power Electron.*, vol. 34, no. 11, pp. 11383–11395, Nov. 2019.
[35] S. M. Hoseinizadeh, S. Ouni, H. Karimi, M. Karimi-Ghartemani, and K. L. Lian, "Comparison of PLL-based and PLL-less vector current controllers," *IEEE J. Emerg. Sel. Topics Power Electron.*, early access, Mar. 17, 2021, doi: 10.1109/JESTPE.2021.3066512.
[36] N. Pogaku, M. Prodanovic, and T. C. Green, "Modeling, analysis and testing of autonomous operation of an inverter-based microgrid," *IEEE Trans. Power Electron.*, vol. 22, no. 2, pp. 613–625, Mar. 2007.
[37] H. Wu, X. Ruan, D. Yang, X. Chen, W. Zhao, Z. Lv, and Q. Zhong, "Small-signal modeling and parameters design for virtual synchronous generators," *IEEE Trans. Ind. Electron.*, vol. 63, no. 7, pp. 4292–4303, Jul. 2016.
[38] J. Suarez, H. M. T. C. Gomes, F. A. J. Sguarezi, D. A. Fernandes, and F. F. Costa, "Grid impedance estimation for grid-tie inverters based on positive sequence estimator and morphological filter," *Elect. Eng.*, vol. 102, no. 3, pp. 1432–1487, 2020.
[39] A. Ghanem, M. Rashed, M. Sumner, M. A. Elsayes, and I. I. I. Mansy, "Grid impedance estimation for islanding detection and adaptive control of converters," *IET Power Electron.*, vol. 10, no. 11, pp. 1279–1288, Sep. 2017.
[40] A. Karimi and G. Galdos, "Fixed-order H_∞ controller design for nonparametric models by convex optimization," *Automatica*, vol. 46, no. 8, pp. 1388–1394, Aug. 2010.
[41] I. D. Landau, R. Lozano, M. M'Saad, and A. Karimi, *Adaptive Control, Algorithms, Analysis and Applications*. New York, NY, USA: Springer-Verlag, 2011.

BEHROOZ BAHRANI (Senior Member, IEEE) received the B.Sc. degree in electrical engineering from Sharif University of Technology, Tehran, Iran, in 2006, the M.Sc. degree in electrical engineering from the University of Toronto, Toronto, ON, Canada, in 2008, and the Ph.D. degree in electrical engineering from the Ecole Polytechnique Fédérale de Lausanne (EPFL), Lausanne, Switzerland, in 2012. From September 2012 to September 2015, he was a Postdoctoral Fellow at EPFL, Purdue University, West Lafayette, IN, USA, Georgia Institute of Technology, Atlanta, GA, USA, and the Technical University of Munich, Munich, Germany. Since 2015, he has been with Monash University, where he is currently a Senior Lecturer and the Director of the Grid Innovation Hub. His research interests include control of power electronic converters, their applications in power systems, and grid integration of renewable energy resources.